NaviGraph: A graph-based framework for multimodal analysis of spatial decision-making

Amit Koren Iton[1], Elior Iton[2], Daniel M. Michaelson[1,3] and Pablo Blinder[1,3] *

[1] Neurobiology, Biochemistry and Biophysics School. Wise Life Science Faculty, Tel Aviv University. Israel
[2] School of Electrical Engineering & Computer Engineering, Iby and Aladar Fleischman Faculty of Engineering, Tel Aviv University. Israel
[3] Sagol School of Neuroscience, Tel Aviv University. Israel

* Corresponding author
pb@tauex.tau.ac.il

Abstract

Recent advances in neuroscience have enabled simultaneous collection of multimodal datasets, including behavioral tracking, physiological signals, and neuronal recordings. Yet most analysis tools process these streams independently, often requiring manual alignment and custom code. This fragmentation limits reproducibility and interpretability at the experiment level, particularly in models where cognitive impairments are subtle, and reflects a broader tendency to analyze behavior as isolated events rather than as a structured process. Topological methods, though successful in other domains, remain underused in behavioral neuroscience, leaving the architecture of decision-making largely unexplored. To address these, we developed *NaviGraph* (Navigation on the Graph), a flexible, open-source pipeline designed to integrate diverse data types into a unified graph-based framework suited for spatial decision-making studies. By modeling decision points as graph nodes and populating them with behavioral, neuronal, and physiological parameters, NaviGraph offers a holistic, multi-layered perspective on cognition, enabling computation of spatial and topological metrics. This approach shifts the focus from isolated modalities to comprehensive interpretation, making behavioral patterns more accessible and easier to validate across datastreams. We applied NaviGraph to a trial-based spatial memory task in a complex maze and uncovered nuanced sex- and genotype-specific differences. In a knock-in model of Apolipoprotein E ε4 (apoE4), the most prevalent genetic risk factor for Alzheimer's disease, females exhibited deficits detectable only through topological metrics, including inefficient navigation and increased visits to decision points, aligning with the heightened cognitive vulnerability observed in female apoE4 human carriers. Wildtype females, in contrast, displayed more direct recall navigation compared to males. To demonstrate NaviGraph's multimodal capabilities, we mapped neuronal activity from head-mounted miniaturized microscope calcium imaging in the retrosplenial cortex, an area extensively involved in path integration, alongside head orientation dynamics and behavioral trajectories onto the graph structure. This unified framework enabled visualization of decision-point-specific neuronal activity patterns, subpopulation dynamics linked to path familiarity, and physiological-behavioral alignment. With its modular architecture, NaviGraph supports diverse maze configurations and data types, providing a holistic, interpretable, and high-resolution tool for spatial navigation and cognitive research.

Introduction

Behavioral experiments are a fundamental component of preclinical animal research, crucial for understanding cognitive processes and assessing therapeutic interventions [1,2]. These tests span a wide range of modalities, from highly controlled, head-restricted setups relying on repeated trials [3,4], to ecologically relevant tasks replicating real-world environments in which animals engage in unrestrained naturalistic behaviors [5–7]. However, balancing behavioral complexity and natural behaviors, while ensuring feasibility in controlled laboratory settings, remains a significant challenge. For rodents, complex mazes help address this by mimicking real-world navigation through sequential decisions, supporting robust learning and memory retention [8]**.** While these designs enable more naturalistic observations in laboratory settings, the most common approach to behavior analysis predominantly relies on what can be described as classic metrics, such as latency, velocity and error rates [9–11]. Though widely applied, these measures don't address relational and structural properties of navigation that are critical for capturing the full complexity of decision-making, and are easily influenced by confounding factors such as stress, motivation, or physical state [12,13]. Topological analysis, which focuses on relational rather than purely spatial properties, has shown value across diverse domains, including transportation and protein folding [14], but remains underexplored in behavioral research, despite its potential to complement the limitations of classic metrics. As a result, the architecture of decision-making often goes unmodeled, and behavior is frequently reduced to isolated events rather than interpreted as a structured process.

These conceptual limitations are compounded by the increasing complexity of modern behavioral setups, which now enable simultaneous collection of multiple parameters during experiments, including neurophysiological [15,16], behavioral [17,18], and physiological [19] data streams. While these innovations have greatly enhanced our ability to study cognition, the diverse nature of these datasets presents significant obstacles [20,21] and the field lacks a unified standard to encompass them all into a single data or object type. Though tools that synchronize behavioral and neuronal data have started to emerge [22], they still lack the ability to integrate data within the same framework in complex spatial designs [23]. As such, there is currently no standardized open-source tool capable of addressing both the integration of diverse data streams into a unified analysis framework, and the limitations of traditional maze analysis measures in structured paradigms.

To address these gaps we developed *NaviGraph* (Navigation on the Graph), a flexible pipeline designed to incorporate diverse data streams within a graph-based framework. At the core of NaviGraph is a topological representation of the maze, where decision points are modeled as nodes and the paths between them as edges. With the synergistic combination of classic and topological approaches, NaviGraph provides a structured yet flexible analysis framework, enabling the integration of multiple data streams and parameters into a cohesive multilayer network [24]. By allowing data to exist within their own layer, while maintaining connectivity between layers through the same graph structure, interactions between diverse data at each decision point can be captured in a straightforward manner, enabling experiment-level interpretation. The pipeline includes modules for data preprocessing, computation of classic behavioral and graph-based metrics, multistream data alignment, aggregation and visualization of results. As we demonstrate, this approach enhances the detection of subtle behavioral and neural patterns, many of which may remain obscured when using traditional or single-stream analysis.

We applied NaviGraph within an automated, trial-based version of the complex binary maze introduced by Rosenberg et al. [8], and implemented a robust learning and memory task, emphasizing minimal human intervention. By leveraging both classic and topological measures, we show how these complementary approaches offer a more comprehensive analysis of complex behaviors in health and disease. We further demonstrate the platform's multistream capabilities by integrating head orientation and neuronal activity from unrestrained calcium imaging with miniaturized microscopes [25], in order to showcase potential for future applications. Overall, NaviGraph's approach provides a valuable tool that leverages the power of graph theory to offer a standardized, flexible and sensitive analysis of spatial navigation and decision-making, enabling multimodal behavioral neuroscience without requiring advanced computational skills or custom infrastructure.

Results

NaviGraph pipeline structure

The workflow of NaviGraph, illustrated in Figure 1, describes the structure of the pipeline and its capability to unify multiple data streams and behavioral parameters within a biologically meaningful graph-based analysis framework. Designed to operate in modular, easy-to-use stages, the pipeline accommodates diverse experimental needs by allowing the flexible integration of additional data following standard preprocessing.

Initially, pose estimation datasets are spatially registered to the maze layout through a calibration and validation process that ensures accurate transformation of raw pixel coordinates into topological representations, namely, nodes and edges of the graph structure. This enables precise mapping of the trajectory onto the graph, which serves as a common scaffold for all subsequent analysis. Within this framework, NaviGraph computes both conventional behavioral metrics (e.g., time to reward and velocity) and graph-based topological metrics (e.g., number of unique nodes traveled and number of nodes on direct path to reward). If available, additional parameters such as synchronized neuronal activity is also mapped onto the graph structure, enabling the identification of node and path specific activity patterns.

As the pipeline progresses, it generates several structured datasets, including indexed positional, neuronal, and physiological data, all stored within the same graph framework. These outputs are automatically aggregated across sessions and experimental groups, allowing seamless comparison of behaviors and neural responses over time and across conditions.

Unlike many currently available pipelines that focus on isolated data modalities or require substantial post-processing, NaviGraph offers an end-to-end, experiment-level analysis approach. Its flexible open-source design supports a wide range of maze layouts and experimental paradigms (Supplementary Fig.1), making it a broadly adaptable tool for behavioral neuroscience research. A more detailed overview of the computational modules and analysis flow is provided in the Methods section and accompanying code repository.

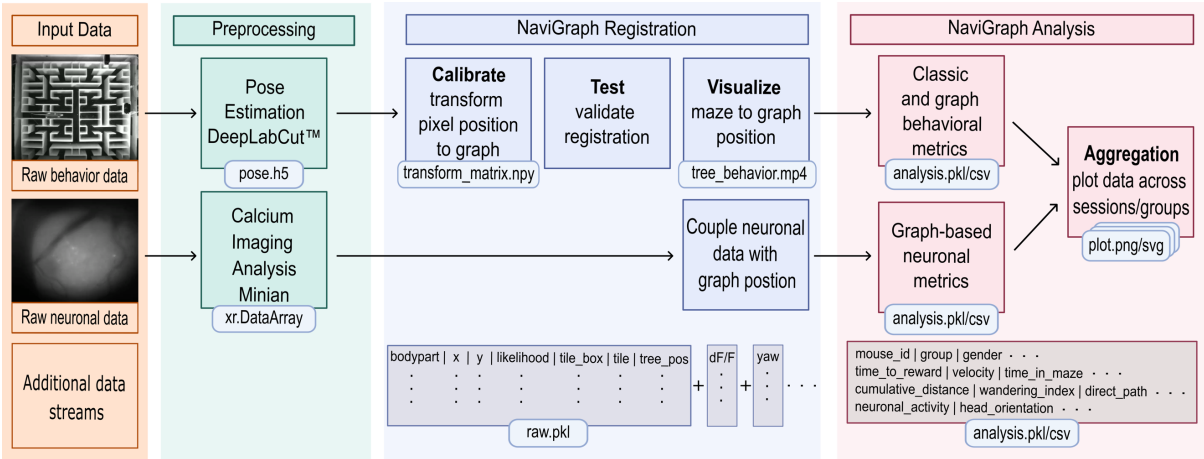

Figure 1: NaviGraph pipeline. *Workflow and file structures for topological behavioral, neuronal and physiological analysis. Color-coded sections represent different stages of the process. Input data: Raw data collection. Preprocessing: Pose estimation and neuronal data generation. NaviGraph registration: Calibration - conversion of pixel positions to maze map and graph coordinates. Validation - testing registration accuracy. Visualization - mapping positions to maze and graph coordinates. Coupling: Neuronal and physiological data integration with maze and graph positions. NaviGraph Analysis: Metric computation - classic and topological behavioral and neuronal metric calculation. Data aggregation - plotting and visualization of results across sessions and groups.*

Behavioral application of NaviGraph

We showcase NaviGraph's ability to analyze behavior with a combination of classic and topological measures (Fig. 2). Our trial-based automated version of the complex maze paradigm [8], was employed to assess learning and memory in male and female C57BL/6 wildtype (WT) mice. In each trial of this task, mice were required to navigate through a series of six correct decisions to a liquid reward port (Fig. 2a). Following one week of self-imposed water restriction (home-cage water was made slightly sour with citric acid, an alternative method to water restriction [26,27]), each mouse completed a learning session which included four consecutive rewarded trials absent of experimenter intervention, followed by a single memory trial 72 hours later. To minimize reliance on spatial cues, the task was conducted in the dark, and maze rotation was applied between sessions. Potential odorant cues from the reward port were masked by placing the liquid rewarded solution around the maze layout.

Time-based trajectories of both female and male WT mice during these spatial learning and memory sessions revealed distinct patterns (Fig. 2b and 2c). An overall shift from broad exploration in the learning session to more efficient navigation in the memory session can be seen. NaviGraph maze coverage metric (Fig. 2d) quantifies this, providing an overview of normalized maze exploration across sessions. In the memory session, we observed a trend that males explored a larger portion of the maze relative to females. Importantly, both sexes show reduced maze coverage in the memory session relative to the learning session, indicating an overall memory retention of the maze structure.

NaviGraph further captures classic behavior metrics such as time taken to reach the reward and average velocity (Fig. 2e,f). The first trial of the learning session (L1) represented each animal's initial exposure to the maze layout, noting that in order to shorten the previously reported exploratory phase [8], animals were introduced to the paradigm via the reward arm. We observed gradual reduction in the time taken to reach the reward across the learning trials in both sexes (Fig. 2e) (*p=0.027 effect of learning trial number; two-way Repeated Measures

(RM) ANOVA). In the memory session (M1), females reached the reward slightly faster than males, but no significant differences between the groups were shown. Both groups displayed significantly shorter times in the memory session relative to the first trial of the learning session (**p=0.001 for females and *p=0.01 for males). In both sexes there was general conservation of velocity through the trials (Fig. 2f). No significant velocity differences were observed between males and females in either session, indicating that speed does not underlie the time-based performance differences.

To contextualize mouse performance in the topological measures, we generated benchmarks for random graph navigation by averaging 5000 random walks on the tree graph, with and without backtracking. Our results revealed that random walks without backtracking, which are allowed to turn around only upon reaching a dead end, yielded an average cumulative path length (total number of nodes visited in each trial) of 485.38 nodes ± standard deviation (SD) 490.98 nodes on their way to the reward location. In contrast, the random walks with backtracking resulted in an average cumulative path length of 1298.14 nodes ± 1365.89. When calculating the "wandering index", referring to the number of novel nodes visited relative to the total number of nodes in the maze, there was less contrast between the backtracking (73.12 ± 35.76) and non-backtracking walks (72.019 ± 35.70). Consequently, the analysis focused on the results from the non-backtracking random walks, as these values aligned more closely with actual behaviors of the mice and provided a more realistic benchmark for evaluating performance.

We show that both cumulative path length and wandering index values of the first learning trial (L1) were comparable to the random walk benchmark, while in the final learning trial (L4) these measures shifted towards the perfect route to the reward. Moreover, the cumulative path length (Fig. 2g) decreased significantly across the learning session, indicating improved navigational efficiency (*p=0.01 for L1-L3 and L1-L4 in females, *p=0.04 for L1–L4 in males; Tukey's post hoc following 2-way RM ANOVA). Similarly, the wandering index (Fig. 2h), also declined progressively (*p=0.017 in females, **p=0.006 in males), further supporting the presence of task learning.

To assess memory retention, we compared performance in the final learning trial (L4) and the memory trial (M1) conducted 72 hours later. No significant differences were found in either cumulative path length or wandering index, indicating that mice retained spatial memory across sessions. Furthermore, comparisons between L1 and M1 demonstrated significant reductions in cumulative path length (**p=0.002 in females; *p=0.02 in males) and wandering index (***p=0.001 in females; **p=0.0006 in males). In the memory session (M1) females showed a trend toward lower exploratory behavior, suggesting slightly more refined recall.

To assess spatial insight of the maze structure, we analyzed the length of the direct path to the reward, defined as the sequence of consecutive correct choices leading to the reward location (Fig. 2i). A longer direct path to the reward indicates fewer mistakes, reflecting a more accurate internal representation of the maze structure [8,28]. This measures reflects the ability to navigate the maze efficiently, suggesting a stronger cognitive map and reliance on learned spatial representations rather than exploratory or random navigation strategies [29,30]. We observed that both sexes showed an overall positive learning curve along the trials of the learning session, which manifested as a gradual increase in the number of nodes on the direct path to the reward. Interestingly, females exhibited longer direct paths to the reward during

the memory session, with fewer deviations compared to males (**p=0.008; Mann-Whitney test), indicating a higher degree of maze structure retention during navigation. This is further supported by the significantly longer direct paths to the reward in females when comparing the recall session to the first trial of the learning session, in which the navigation was more random (**p=0.0021).

A key feature of NaviGraph is the ability to topologically visualize behavior on the graph itself. Here, we display decision confidence and visit counts on the binary tree representing the maze (Fig. 2j,k), where the size of each node corresponds to the mean visit frequency to said decision point, and color intensity to the mean confidence index, calculated as the difference between correct and incorrect turns relative to the total number of turns per node. The confidence index illustrated that during the memory session, females (Fig. 2j) display greater decision-making confidence particularly in nodes leading to the reward. In contrast, males (Fig. 2k) show lower confidence on this path in the memory session. Furthermore, these graphs allow node-specific visualization of patterns quantified by the topological measures. For example, the reduced node visitation in females during the memory session which was quantified in the cumulative path measure. Overall, NaviGraph's topological metrics revealed gender-specific behavioral effects even with a small sample size, completing indistinct trends displayed by classic measures.

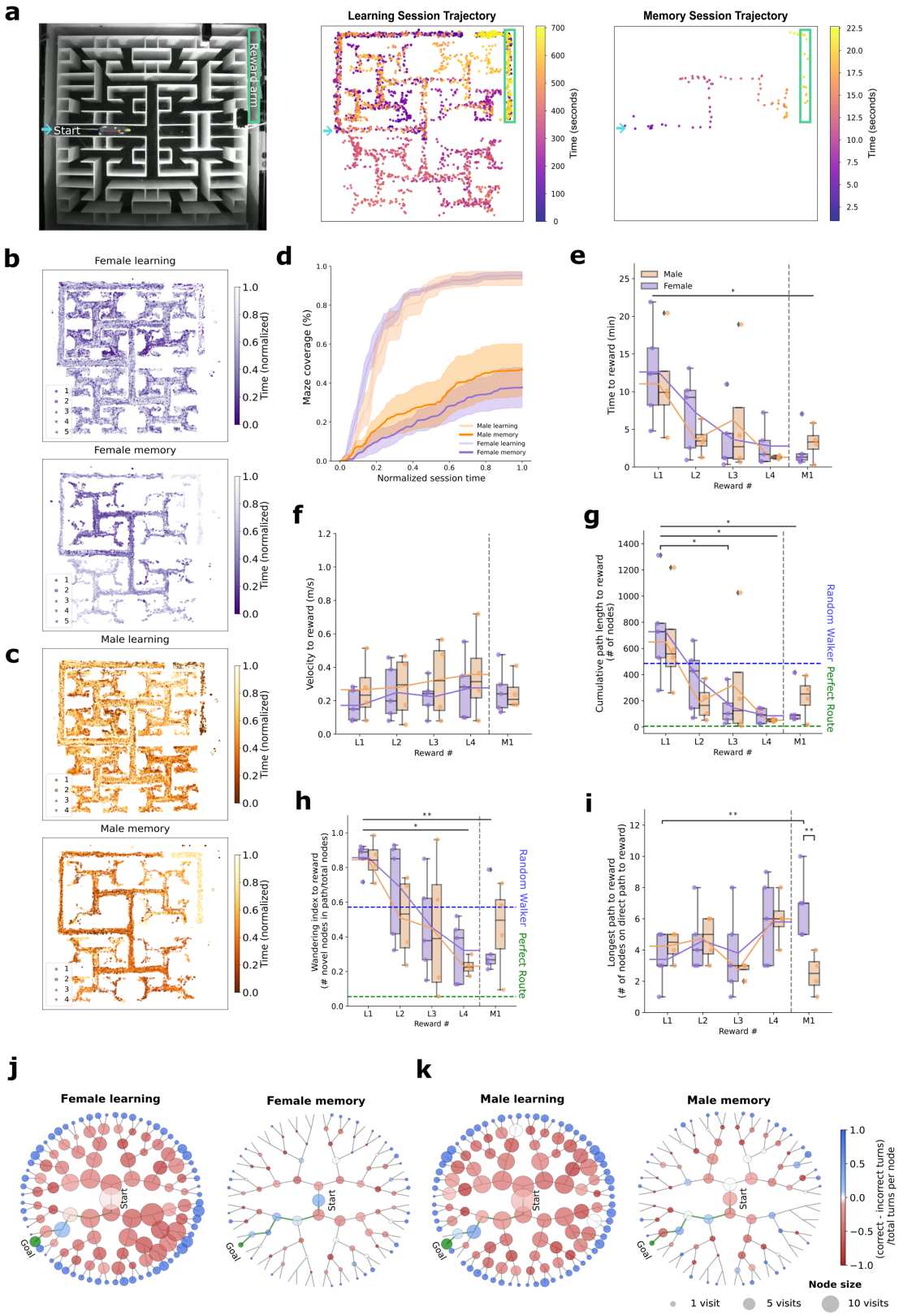

Figure 2: NaviGraph synergistic topological and classic behavioral analysis in male and female wildtype mice. *(a) Complex maze paradigm. Left: Maze structure. Middle: Representative learning session trajectory. Right: Representative memory session trajectory. Entrance and reward arm indicated by blue arrow and green box respectively, time progression depicted by colorbar. (b, c) Trajectories over session time. Normalized trajectories*

*of individual C57BL/6 wildtype (WT) n=5 female (b) and n=4 male (c) mice in learning (top) and memory (bottom) sessions respectively. (d-i) NaviGraph metrics. Females and males shown in purple and orange, respectively. Four consecutive learning session trials represented by rewards L1-L4; memory session represented as M1. (d) Maze coverage during normalized session time, shown as mean ± SEM. (e) Time taken to reach the reward. (f) Average velocity to the reward. (g) Cumulative path: total number of nodes passed to reach reward. Average of 5000 random walker bouts on the graph depicted by the blue dashed line. Direct path to reward depicted by green dashed line. (h) Wandering index: number of unique nodes passed. (i) Longest path to reward: number of nodes passed on the direct path to the reward. Data in box plots depicted as median ± interquartile range, lines reflect group means; * p<0.05. (j, k) Confidence index and node visits shown on the binary tree representing the maze. Decision confidence levels, calculated as the difference between mean correct and incorrect turns relative to the total number of turns per node, for females (j) and males (k) during learning and memory sessions. Node sizes represent mean group visit frequency to each node, and color intensity denotes the confidence index.*

Topological metrics uncover ApoE4-related memory deficiencies

NaviGraph's topological behavior analysis was applied to a well-established humanized mouse model of the most prevalent genetic risk factor for Alzheimer's disease (AD), Apolipoprotein E ε4 (apoE4) [31], given its typically mild behavioral phenotype [32,33] (Fig. 3a). Male and female apoE4 mice were compared to control mice expressing the apoE3 isoform, which is considered the benign variant associated with normal cognitive function [31,32]. ApoE4 and control apoE3 mice underwent a learning session (four rewarded trials) followed by a memory session 72 hours later (single rewarded trial), as described in the previous section. To assess general exploration patterns, we first examined maze coverage (Fig. 3b,c), which quantifies the percentage of the maze explored over normalized session time. All mice demonstrated broader maze exploration during the learning session compared to the memory session, indicating increased task familiarity and more focused navigation during the latter. Female apoE4 mice exhibited higher maze coverage during both the learning and memory sessions compared to other groups.

To reduce visual complexity and emphasize the differences from the beginning to the end of the learning session, only the first and final learning trials are presented in the main behavioral metrics of Figure 3, while all reward trials are included in the supplementary figures for comprehensive analysis (Supplementary Fig. 2). As can be seen, the conventional behavioral metrics of time taken to reach the reward and average velocity (Fig. 3d,e), did not reveal significant genotype or sex differences across trials. In the time to reward (Fig. 3d), a trend was observed where female apoE4 mice took longer to reach the reward compared to control apoE3 mice in the memory session, but these differences were not statistically significant. Notably, all groups displayed significantly higher velocity during the memory session compared to the final trial of the learning session (***p=0.0003 effect for trial number; mixed-effects 2-way ANOVA analysis between the L4 and M1 rewards) (Fig. 3e).

In contrast to conventional measures, topological metrics captured task learning through within session improvements. Specifically, the cumulative path length decreased significantly between L1 and L4 (**p = 0.007; Mixed-effects model fixed effect for trial number) (Fig. 3f), alongside more direct trajectories (**p = 0.009) (Fig. 3h). No significant genotype or sex effects were detected within the learning phase. To assess memory retention, we compared L4 to M1 performance. ApoE4 females exhibited a significant increase in direct path length during the memory session compared to the final learning trial (**p=0.006; Tukey's post hoc), suggesting impaired spatial memory. In contrast, apoE3 mice and apoE4 males did not show significant

differences, indicating more preserved memory in these groups. Additionally, comparisons between L1 and M1 showed residual improvement across sessions in all topological navigation measures (fixed effect for the session in a Mixed-effects model of L1 vs. M1; **p=0.009 for cumulative path length, *p=0.036 for wandering index, *p=0.033 for direct path length).

Topological metrics further captured group-specific differences in memory performance during the recall session (M1), particularly highlighting deficits in apoE4 female mice. The longest path to the reward, which represents the sequence of correct decisions to the goal (Fig. 3h), differed significantly between groups (*p=0.041, Kruskal-Wallis test). ApoE4 females followed significantly less direct routes to the reward compared to apoE3 females (*p=0.023) and apoE4 males (*p=0.026), suggesting impaired recall of the maze structure. A similar pattern emerged in the cumulative path length (Fig. 3f), with apoE4 females visiting significantly more nodes on the route to the reward than apoE3 females (*p=0.05) and apoE4 males (**p=0.005), indicating reduced navigational efficiency. The wandering index (Fig. 3g), which reflects the extent of exploratory behavior by the proportion of unique nodes visited, further supported these findings. During the memory session, apoE4 females exhibited wandering indicies approaching those observed in random walk simulations (see previous section), in contrast to apoE3 males (**p=0.0025) and with a trend toward significance relative to apoE3 females (p=0.055), both of which showed more focused navigation. Overall, significant differences were observed between groups in this measure during the memory session (*p=0.025), reinforcing the presence of genotype and sex-specific apoE4 memory impairments in topological navigation behavior.

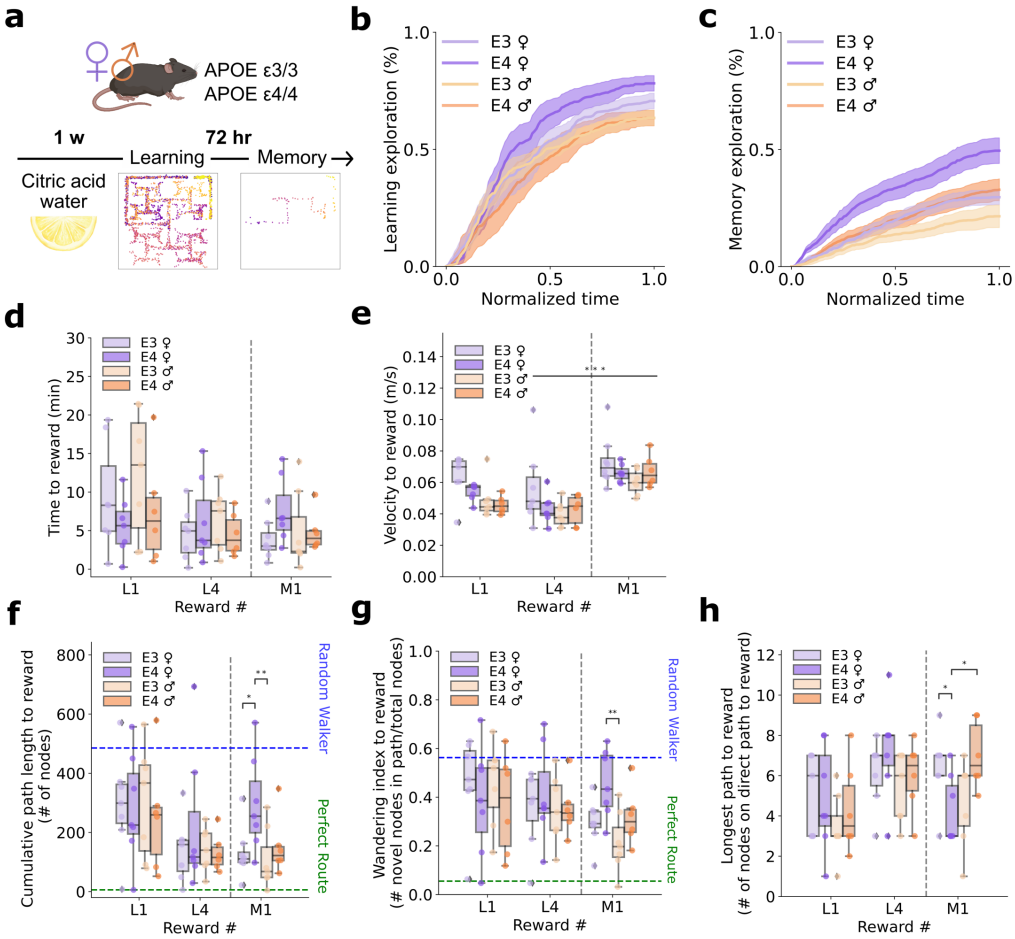

Figure 3: NaviGraph topological analysis uncovers behavioral nuances in an apoE4 Alzheimer's disease model. *(a) Experimental design. (b, c) Maze exploration. Mean percentage of maze explored over time, normalized to either Learning (b) or Memory (c) session durations. (d-h) NaviGraph behavioral classic and topological metrics: (d) Time to reward. (e) Average velocity to the reward. (f) Cumulative path length, total number of nodes passed to reach reward. Average of 5000 random walker bouts on the graph depicted by the blue dashed line. Direct path to reward depicted in green dashed line. (g) Wandering index, number of unique nodes passed to reach reward. (h) Longest direct path to reward, number of graph nodes passed on the direct path to the reward. Plots depict results for first and last rewards in learning session (L1, L4) and reward in memory session (M1). Females and males shown in purple and orange, respectively, apoE4 genotype in darker shades. Data depicted as median ± interquartile range for apoE4 and control apoE3 targeted replacement 5-month-old female (n=7-8) and male (n=6-7) mice.; * p<0.05, ** p<0.01, *** p<0.001.*

To further characterize these phenotypes, visual representation of decision confidence and visit frequencies were generated. Similarly to the previous section, the confidence index is calculated as the difference between the mean correct and incorrect turns divided by the total number of turns made from each node (Fig. 4). The relationship between the confidence and visit frequency distributions is shown by linear regression.

In the first trial of the learning session (Fig. 4a), no significant changes were observed between groups in either visit frequencies to decision points, or confidence index values. Regression analysis for the relationship between both distributions, revealed the steepest slope in apoE4 males (−0.2341), indicating a more pronounced reduction in confidence index value with increasing visit counts, similarly to apoE3 females (−0.2155). ApoE3 males (−0.1287) and apoE4 females (−0.1166) displayed a similar more shallow decline.

During the final trial of the learning session, apoE4 females displayed significantly higher visit counts compared to all other groups, including apoE4 males (****$p < 0.0001$), apoE3 females (**$p=0.005$), and apoE3 males (*$p=0.012$), as shown by the Kolmogorov-Smirnov test. However, no significant differences were observed in confidence index values across any group. Regression analysis of the distributions in the final learning trial (Fig.4b) highlighted that apoE4 males exhibited the steepest decline in confidence with increasing visit counts (−0.426), followed by apoE3 females (−0.234), apoE4 females (−0.177) and apoE3 males (−0.173). The random walk regression slope displayed the shallowest decline (-0.043) of the regression slope, and significantly differentiated from all groups in both the visit counts and confidence index values.

In the memory session as well (Fig. 4c), apoE4 females showed significantly higher visit counts compared to apoE4 males (**$p=0.007$), apoE3 females (***$p < 0.001$), and apoE3 males (**$p=0.003$; Kolmogorov-Smirnov). Similar to the final learning session, regression slopes indicated a consistent reduction in confidence index with increasing visit counts across all groups. ApoE3 males exhibited the steepest slope (−0.245), followed by apoE4 males (−0.229), apoE3 females (−0.201), and apoE4 females (−0.188). Interestingly, in both the final learning session and the memory session, apoE4 females displayed relatively gradual slopes. Overall, these patterns reinforce the observed behavioral impairments in apoE4 female mice highlighted by previous topological measures, underscoring the ability of graph-based analysis to reveal subtle cognitive deficits.

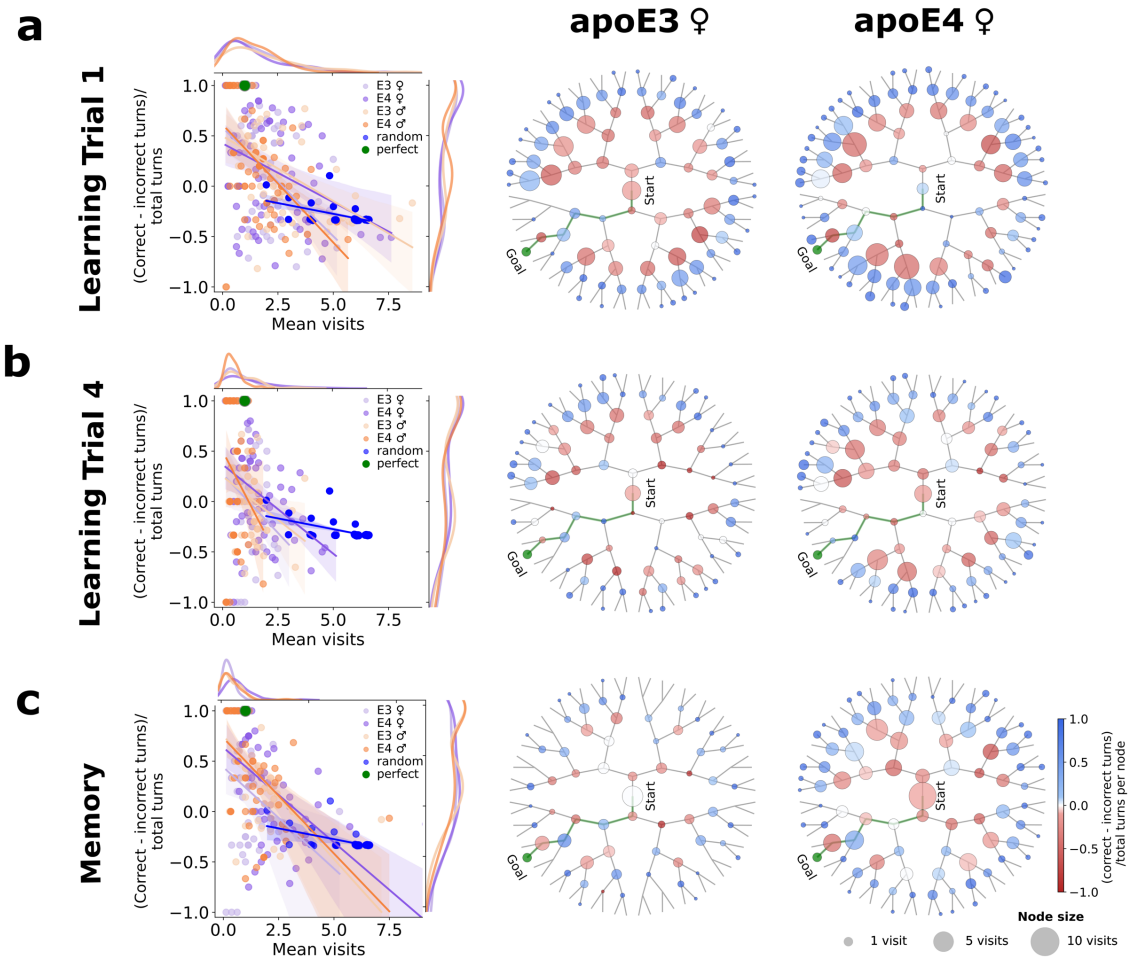

Figure 4: Topological analysis of navigation confidence and visit frequencies in apoE mice. *(a) First learning trial. (b) Final learning trial. (c) Memory session. Left panel: Node decision confidence and visit frequency distribution relationships. Confidence index is calculated as the difference between mean correct and incorrect turns relative to the total turns made from each node. Steeper negative regression slopes indicate less confidence with increased visits. Females and males are shown in purple and orange, respectively, with apoE4 genotype in darker shades. Averages of 5000 random walker bouts depicted in blue, perfect path to reward depicted in green. Middle and right panels: Confidence index and visits per node displayed on the binary tree representing the maze, for apoE3 (middle panel) and apoE4 (right panel) female mice. Node size corresponds to the mean number of visits and color intensity reflects decision confidence. Data from apoE4 and control apoE3 targeted replacement 5-month-old female (n=7-8) and male (n=6-7) mice.*

Topological neuronal, physiological and behavioral data integration

NaviGraph's ability to integrate behavioral, neuronal and physiological data is exemplified in Figure 5, showcasing the potential to analyze these within a graph-based framework. During exploration of the complex maze, calcium signals and head angles were recorded with a miniaturized microscope [25,34] in the retrosplenial cortex (RSC) (Fig. 5a), an area extensively involved in spatial cognition and navigation [35]. As can be seen, we showcase the pipeline's ability to map this diverse data onto behavioral decision points. A general heatmap of neuronal activity over time as well as representative neurons (Fig. 5b) demonstrate how neural activity can be tracked throughout the navigation of the maze, capturing fluctuations across different

decision points. A comparison of population activity between movement and stationary periods indicates an increase in neuronal activation during movement (****$p<0.0001$; paired two-tailed Student's t-test, n=43) (Fig. 5c).

NaviGraph enables the direct mapping of neuronal activity onto the nodes and edges of the graph structure that represent the maze layout (Fig. 5d); with nodes representing binary decision points. In this representation, node size corresponds to visit frequency and color intensity reflects the average neuronal activity, seen by change in calcium signal fluorescence at each decision point. This graph-based approach offers a straight-forward way to both analyze and visualize how specific maze locations elicit varying degrees of neuronal engagement.

This perspective also allows looking at neuronal responses during repeated visits to specific nodes that build a defined path (Fig. 5e). By visualizing heatmaps of neuronal activity along repeated visits to the same path, it is possible to observe the consistency or variability of activity across different navigation episodes. This can enable tracking how specific neuronal populations adapt firing patterns based on increasing familiarity with the environment, potentially revealing dynamic changes along learning sequences of spatial decisions. We performed hierarchical clustering (Ward's method) to uncover natural groupings of neuronal activity patterns across visits to the same nodes. The resulting dendrogram provides a visual arrangement of clusters based on similarity in activity patterns over the course of the animal's separate visitations to the same path. Additionally, a more granular analysis of the top three clusters was employed across nodes and iterations (Fig. 4f). Significant differences were observed across all iterations and nodes between Cluster 3 and Cluster 1, with p-values consistently below 0.005 (Mann-Whitney U test with a Bonferroni correction for multiple comparisons of clusters). Additionally, significant differences between Cluster 2 and Cluster 3 were observed only in the first iteration (all nodes; ****$p<0.0001$), while non-significant differences were found in later iterations ($p>0.4$). Comparisons of Cluster 1 and Cluster 2 captured highly significant differences across iterations 2-4 for all nodes (****$p<0.0001$). These results point to likely different activity patterns between the clustered neuronal subpopulations during repeated navigations along a distinct path, possibly suggesting a functional heterogeneity within the RSC that may be further explored in the future.

In addition to neuronal data, NaviGraph can integrate additional data streams recorded simultaneously with the mouse location and neuronal activity. For example, we incorporate head orientation metrics. Here, yaw angles were extracted from head orientation data (see Methods section) and mapped onto the graph representation of the maze spatial coordinates. We demonstrate topological representations of mean head orientation along distinct paths (Fig. 5i) and decision points (Fig. 5j), to exemplify how mouse orientation data can align with neuronal activity and behavioral choices, providing a rather holistic view of goal directed and exploratory behaviors. Overall, we presented NaviGraph's ability to integrate and visualize multi-modal data - including behavior, neuronal activity, and physiological parameters - into a unified analytical framework. This approach offers a novel perspective for tracking changes in neuronal encoding and behavior over time, as well as revealing patterns of plasticity and adaptation as the structure of the environment is being learned and later retrieved.

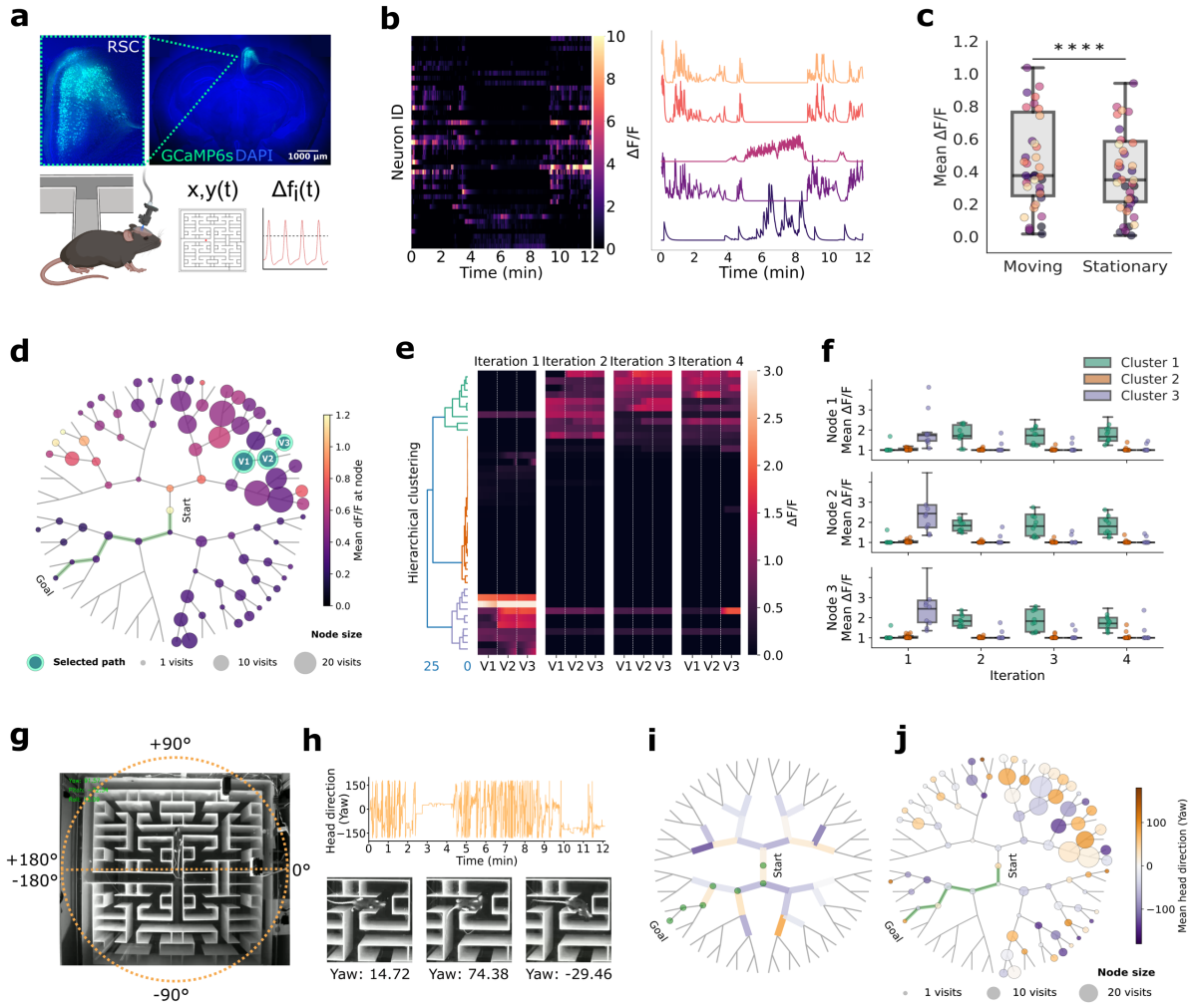

Figure 5: Topological integration of behavioral, neuronal and physiological data. *(a) Experimental setup for simultaneous recording of calcium signals in the retrosplenial cortex (RSC) with miniature microscopes during complex maze exploration (created with BioRender [36]). Top panel: Coronal section of the AAV1.Syn.GCaMP6s injection site in the RSC; GCaMP6s labeled neurons (green), tissue stained with DAPI (blue). (b) Population (left) and representative individual neuron (right) activity over time during maze navigation. (c) Mean neuronal activity of individual neurons during movement versus stationary episodes. (d) Graph representation of the binary tree maze structure. Nodes represent decision points, node size proportional to visit frequency and color intensity reflects mean neuronal activity. (e) Heatmaps of neuronal activity for repeated navigations in a specific path, depicted as nodes V1, V2 and V3 in (d). Hierarchical clustering (Ward's method) highlights distinct neuron clusters through activity patterns. (f) Neuronal cluster subpopulation activity during repeated navigation bouts to the same path. Cluster 1 n=10, Cluster 2 n=23, and Cluster 3 n=9. Boxplot data shown as median ± interquartile range; **** p<0.0001. (g) Maze structure with overlaid head direction reference angles. (h) Time-series of head orientation (yaw) throughout maze exploration, with representative directions depicted in the bottom panel. (i, j) Graph representation of mean head direction at edges (i) or nodes (j), reflected by color intensity, with node size representing visit frequency.*

Discussion

We introduced here NaviGraph, a flexible graph-based analysis pipeline designed to capture the intricacies of spatial decision-making and behavior in mazes of varying layout. This approach responds to two ongoing challenges in behavioral neuroscience: the tendency to analyze behavior as isolated, time-point events, and the fragmentation of multimodal data across separate analytical pipelines. Conventional analysis often treats actions like zone entries or reward collection as discrete outputs, while neural or physiological signals are typically aligned to these events without considering the task's structural context. NaviGraph addresses these by modeling spatial tasks as graphs, where decision points form nodes and transitions form edges, embedding behavioral, neuronal, and physiological data streams within a unified topological framework. This enables behavior to be interpreted as structured paths, offering a more nuanced perspective on cognition. In addition, the pipeline was designed with usability in mind. Many existing frameworks generate outputs that require extensive post-processing and custom scripting to extract group-level biological insights. NaviGraph streamlines this process, offering an end-to-end modular workflow that produces interpretable results, while minimizing the need for advanced computational expertise.

We applied NaviGraph to both wild-type and Alzheimer's disease (AD) risk factor apoE4 knock-in mice and demonstrated its ability to uncover subtle phenotypes not captured by conventional metrics alone. By reinforcing classic behavioral metrics such as time and velocity with topological measures, NaviGraph provides a powerful platform for studying both healthy and pathological behaviors. We also demonstrated the integration of neuronal calcium imaging and head orientation dynamics with behavioral trajectories, highlighting NaviGraph's ability to unify diverse data within a structured spatial context.

Graph-based behavioral analysis

To demonstrate NaviGraph's topological approach, we developed a trial-based and automated version of the naturalistic complex maze introduced by Rosenberg et al. [8], and tracked mice behavior during a learning session and spatial memory recall session 72 hours later. This design, analyzed through NaviGraph's synergistic combination of classic and graph-based topological metrics, allowed us to dissect behavioral changes in the complex maze across trials and between sessions. We interpreted spatial learning and task acquisition as the improved progression of behavior across the learning session trials. Spatial memory, in contrast, was assessed by comparing the final learning trial to the memory trial. If performance in the memory trial remained consistent with the final learning trial, we inferred successful memory retention. In contrast, a decline in performance was taken as indicative of impaired memory recall.

In WT mice, we validated this paradigm by demonstrating a clear learning effect across trials, indicating progressive acquisition of the maze structure and improved efficiency of decision-making over time. Although this cohort was small and primarily intended to showcase NaviGraph's capabilities, the analysis highlighted sex-specific navigation patterns, particularly during the memory phase. While both sexes explored the maze extensively and similarly during the learning session, males displayed slightly higher maze coverage in the memory session, reflecting less efficient recall (Fig. 2). Spatial memory retention was topologically quantified using the sequence of consecutive correct decisions made to reach the reward. The

longer the direct path to the reward, the fewer mistakes were made, a result interpreted as enhanced spatial memory [8,28]. In the memory session, females followed longer uninterrupted direct paths to the reward with fewer deviations compared to males (Fig. 2i), suggesting a more accurate recall of the maze structure. Notably, these experiments were conducted in the dark, minimizing reliance on visual cues. This may have resulted in greater dependence on egocentric navigation strategies, which rely on self-movement and proximal cues [29,37,38]. Previous reports suggest that males tend to use allocentric strategies during navigation and exploration, relying on external cues to form cognitive spatial maps of their environment, whereas females often rely on egocentric strategies [39,40]. This could, in part, explain the more efficient navigation to the reward observed in females during the recall session, as females adapt more flexibly to tasks when external cues are limited [41].

To contextualize performance within topological measures, we generated benchmarks for random navigation through averaging 5000 random walks on the maze tree graph to the reward location, both with and without backtracking. Interestingly, non-backtracking random walks, which prevent revisiting nodes unless a dead end is reached, more closely resembled the navigation patterns we observed in mice. These values were subsequently used as performance benchmarks in our analysis. This observation aligns with well-established findings that animals often avoid revisiting previously explored locations to optimize navigation efficiency [8,29,42,43], a behavior indicative of forward planning and effective exploration driven by hippocampal mechanisms that support goal-directed planning and optimal path encoding [44,45]. Such characteristics are reflected more accurately by non-backtracking models. This demonstrates NaviGraph's ability to seamlessly compare real-world behaviors to computational models on the same graph, allowing for the natural identification of navigation patterns and deviations. For example, in WT male and female mice, performance during the first learning trial (L1), as measured by the total number of nodes visited and the number of unique nodes traversed per trial, appeared comparable to the random walk benchmark, consistent with the first exposure to the maze and a lack of prior spatial knowledge. By the final learning trial (L4), both measures showed a visible shift toward values more closely resembling a direct, efficient route, suggesting a transition from exploratory to goal-directed behavior over the course of the learning session.

An additional innovation enabled by the topological approach to behavior is the ability to visualize behavioral patterns directly on the maze's graph structure. This capability provides a visually intuitive and detailed representation of navigation strategies, decision-making, and efficiency, offering insights that extend beyond traditional summary metrics (Fig. 2j,k). We computed a "Confidence Index" measure to quantify decision-making accuracy at each node within the maze relative to the reward location. This index was calculated as the difference between correct and incorrect turns from a given decision point, normalized by the total number of turns taken at that node. For instance, a node with a confidence index approaching 1 indicates highly consistent correct decision-making, while values near 0 suggest random choice behavior, and -1 portrays consistent incorrect decisions. This metric allows pinpointing specific areas where navigation falters or excels, offering a fine-grained visual analysis of behavior with both spatial and temporal precision. In this experiment, female WT mice displayed greater decision-making confidence and less node visitation relative to males in nodes leading to the reward during the memory session. The continued exploration observed in male memory sessions may reflect less effective strategy adaptation or learning under these

conditions. These patterns demonstrate the approach's sensitivity, aligning with the notion that topological structure plays a key role in spatial decision-making [46].

Building on this, we applied NaviGraph to a disease model using apoE4 knock-in mice, carrying the most prevalent genetic risk factor for AD [31]. In this model, a mild behavioral phenotype and heightened sensitivity to stress is usually exhibited, limiting the efficacy of traditional assays and measures in detecting apoE4-mediated cognitive decline [32,33,47], specifically in young and middle-aged mice [48,49]. We compared 5-month-old male and female apoE4 mice to control mice expressing the apoE3 isoform, which is considered to be the benign variant associated with normal cognitive function [31]. Despite a lack of significant differences in classic metrics such as time taken to reach the reward, NaviGraph uncovered marked disruptions in topological metrics of apoE4 females (Fig. 3), aligning with a large body of evidence indicating that female apoE4 carriers are at a significantly higher risk for cognitive decline and AD compared to males [50,51]. Specifically, we observed less efficient paths to the reward location, higher wandering indices, and lower decision-making confidence during the memory session of apoE4 females. In contrast, apoE4 males demonstrated relatively preserved navigation abilities, performing more similarly to apoE3 mice across several metrics. These findings are in agreement with previous studies showing that apoE4 males are often less affected by spatial memory impairments than females, which show increased vulnerability to AD-related neuropathology, including amyloid-beta plaque accumulation and synaptic dysfunction [48,51,52].

NaviGraph further captures group-specific patterns by populating the graph nodes with diverse behavioral parameters such as the confidence index and visit frequencies (Fig. 4). ApoE4 females exhibited the highest visit counts during the memory session, significantly differing from apoE4 males and both apoE3 control groups. Interestingly, uniformly negative regression slopes across all groups were observed, suggesting a shared behavioral pattern: confidence is decreased in nodes where visit frequency is higher. However, the differences in the steepness of these slopes between groups highlight varying degrees of sensitivity to this dynamic, with apoE4 females usually exhibiting more gradual decline. The increased decision point visits observed in apoE4 females could partly explain their less steep regression slope, as a higher number of visits inherently dilutes the contribution of each individual turn (correct or incorrect) to the confidence index calculation, leading to a less dramatic decline in confidence as visit counts increase. Overall, our results strengthen the finding that apoE4 females exhibit more pronounced deficits in spatial navigation. Interestingly, these findings diverge from the WT group, where females outperform males in navigation efficiency. While this finding is based on a small sample, it may reflect the broader observation that the apoE4 allele exacerbates cognitive decline in females more than in males, potentially altering sex-based differences observed in healthy mice.

Taken together, these results underscore the advantage of ecologically relevant tasks combined with a topological analysis approach to detect subtle cognitive phenotypes and highlight the potential of NaviGraph as a tool for revealing impairments in disease models where traditional behavioral measurements alone may fall short, such as apoE4 knock-in mice [32,33]. This framework supports high-resolution behavioral analysis under minimal conditions, including limited trials and small cohorts, without imposing constraints on either. Its flexibility accommodates both short-session designs, critical for models with reduced task tolerance,

and extended protocols suited for longitudinal studies, including those involving neuronal recordings such as calcium imaging or electrophysiology.

Neuronal and physiological data integration

A key component of NaviGraph is its ability to incorporate additional data streams, such as neuronal activity and physiological data, to the same graph-based framework. Here, we showcased the integration of behavioral, neuronal calcium imaging and physiological head orientation data during maze exploration. Neuronal activity was imaged via miniaturized miniscopes [25] in the retrosplenial cortex (RSC), which has been shown to play a critical role in path integration and spatial navigation, particularly in tasks involving egocentric strategies [53,54] lacking visual cues [55,56]. We demonstrated the feasibility of mapping neuronal activity and head direction angles to specific decision points within the maze, translating these into nodes and edges on the graph for correlation with behavioral data (Fig. 5). We observed fluctuations in calcium transients across nodes, enabling a granular view of neuronal activity during spatial decision making. Specifically, we demonstrated the ability to track this across repeated visits to the same paths, to study how neuronal activity or physiological parameters can shift with experience and familiarity. For example, hierarchical clustering revealed neuronal subpopulations which displayed varying activity relative to path familiarity, showing the potential of this approach for future comparison of neuronal activity across different behavioral states, such as exploration and goal-directed behavior. Moreover, NaviGraph provides solid ground for detecting "insight moments" or shifts in strategy [8,28], where neuronal activity aligns with a more efficient or learned path. Such findings could help elucidate how different cognitive states, such as task engagement or spatial learning, emerge at the neural level in health and disease.

Future directions and conclusions

We demonstrate NaviGraph's potential for uncovering subtle behavioral, neuronal and physiological phenotypes, however this study primarily aims to showcase our approach concept and potential use cases. While we integrate a limited sample of neuronal, behavioral and head orientation data from the retrosplenial cortex, future studies could apply the pipeline to larger datasets and additional brain regions involved in key processes like decision-making and memory consolidation [57]. Moreover, additional data streams such as other physiological or metabolic readouts could be naturally incorporated to this framework, enabling a more holistic approach. NaviGraph allows for applications beyond rodent models, with potential extensions to any experiment involving decisions in a predefined spatial layout. Flexible design enables future studies to leverage it across various tasks and imaging techniques, such as integrating data from mini 2-photon microscopes [15], or electrophysiological recordings [58,59].

In summary, we introduce a graph-based topological framework as a powerful and complementary approach to classical behavioral analysis of spatial decision-making. NaviGraph is a flexible, open-source tool that enables comprehensive exploration of multiple layers of information. By integrating diverse data streams - behavioral, neuronal, and physiological - within a unified graph structure, NaviGraph offers a high-resolution, biologically meaningful lens through which to study behavior. This framework enhances the sensitivity and interpretability of behavioral analysis and provides a novel, scalable platform for uncovering cognitive dynamics and deficits in both health and disease.

Methods

Mice

All procedures were approved by the Tel-Aviv University Animal Care Committee (permit number 04-20-060), and every effort was made to minimize animal stress and usage. Animals were housed under standard vivarium conditions; 22°C±1°C, 12-hour reverse light/dark cycle allowing behavioral testing during their subjective night, with *ad-libitum* food and water (see Behavior measurements section). General behavioral assessments were conducted on 3-month-old C57BL/6 mice (n = 4 males, n = 5 females). For Alzheimer's model experiments, we used apoE targeted replacement mice, in which the endogenous murine APOE gene was replaced by human apoE3 or apoE4. These mice were obtained from Taconic Laboratories (Germantown, NY) and were homozygous for the ε3 or ε4 alleles, as previously described [60,61]. Genotypes were confirmed by polymerase chain reaction (PCR) analysis. Behavioral testing was performed on 5-month-old apoE mice (n = 7-8 females, n = 6-7 males). Simultaneous behavioral and neuronal data were collected from a single 8-month-old female.

Behavior measurements

We developed and calibrated an automated, rewarded trial-based complex maze task based on the design of Rosenberg et al. [8]. This maze is optimized to produce a strong spatial learning task with minimized human intervention. The paradigm requires mice to make six correct binary decisions to access a liquid reward. The reward consists of ~5 μL of a 10% sucrose water solution administered to the reward port via an automated syringe pump [62] (see supporting data and Supplementary Fig. 3). Two Arduino-based automated doors with infrared (IR) movement sensors ensure unidirectional navigation post-reward to the start of the maze, allowing the next trial to begin immediately without extra handling (see supporting data for further details). Open test tubes containing 10% sucrose solution were strategically placed around all sides of the maze as a control to eliminate odor cue-based navigation. Between trials, the maze was thoroughly cleaned with 70% ethanol to ensure no residual odor cues. The maze was rotated 180° between learning and memory sessions to prevent spatial cues. All behavioral testing was executed during the mice's subjective night under IR illumination, in a self-contained light-free chamber designed for this apparatus (Supplementary Fig. 3). Behavioral imaging for the apoE experiments was acquired via Thorcam software, while general and neuronally synchronized experiments utilized a Blackfly S FLIR camera.

To motivate the mice to perform the task and minimize stress, an alternative method to water restriction was used [26]; 1 week prior to behavioral testing home-cage water was replaced with water containing 1% food-grade citric acid (CA) (LD Carlson). This method has been previously shown to maintain stable weight and health without impacting behavioral performance [26,27]. Mice had *ad-libitum* access to CA water, and body weights were monitored daily from the onset of exposure through the completion of behavioral testing. Mice were handled and monitored by the behavior testing experimenter. Behavioral testing involved two independent sessions. In the learning session, each mouse was introduced to the apparatus through the reward arm receiving a baseline reward, followed by four rewarded trials or a maximum of 90 minutes. 72 hours later a memory session was conducted. Mice were allowed one rewarded trial or a maximum of 30 minutes. Mice that did not complete the full set of session trials within the allotted time were excluded from further analysis.

Viral injections and cranial windows

Viral vector injections and cranial window surgeries were conducted as previously described [63]. Briefly, mice were anesthetized with isoflurane (5% for induction, 1.5% for maintenance) and given dexamethasone (2 mg/kg intramuscularly) and carprofen (5 mg/kg intraperitoneally) for inflammation control and analgesia. Mice were positioned in a stereotaxic frame (Kopf), with body temperature maintained at 37°C. A 3 mm craniotomy was performed over the RSC of the right hemisphere, centered at 2.5 mm posterior to bregma and 0.5 mm lateral to the midline, using a high-speed manual drill (Osada, drill bit 005 Gebr. Brasseler), with intermittent cooling by artificial cerebrospinal fluid (ACSF). An adeno-associated viral vector expressing GCaMP6s (Syn.GCaMP6s.WPRE.SV40, AV-1-PV2824; titer: ~3.6×10^{12}; UPenn Vector Core) was diluted (1:2 ratio) with ACSF and injected into the RSC at two depths (-450 µm and -250 µm from the pial surface) using a glass micropipette (1 mm outer diameter and a 0.5 mm inner diameter (BF100-50-10, Sutter Instrument) pulled using a micropipette puller (P-2000, Sutter Instrument) to a final tip thickness of 20 to 45 µm). ~400 nL of viral solution was delivered at each depth with pulses of 20 ms at a pressure of 20 psi using a PicoSpritzer II (Parker Hannifin). The micropipette was left in place for 10 minutes post-injection to allow for diffusion and prevent backflow, and 5 minutes between injection depths. A 3 mm coverglass was placed above the cranial window and sealed with glue (Loctite 401) surrounded by black dental cement (Ortho-Jet). The area was then covered with silicone (Ecoflex) to prevent damage to the window. Dexamethasone and carprofen were administered for 3 days following surgery as described above.

Miniscope Ca2+ imaging

Four weeks following the viral injections, mice were anesthetized once more as described above and a miniature microscope (UCLA V4 Miniscope, Open Ephys Production Site, RRID:SCR_021480) [34], attached to its aluminum baseplate, was positioned over the cranial window. The field of view was optimized by focusing on blood vessels and cellular structures. Once the view was confirmed, the baseplate was cemented into place, and the miniscope was detached for future use during imaging sessions. Following base-plate placement, mice were put on a 1% CA water regimen, as described above. Mice were switched to a reverse light cycle, handled daily and habituated to the miniscope for five days in a circular arena within the same environment as the behavioral testing. During testing, animal positions were tracked and synchronized offline with miniscope data as described in the sections below.

Tissue Processing

Mice were euthanized via an intraperitoneal injection of pentobarbital (150 µL) and transcardially perfused with phosphate-buffered saline (PBS), followed by 4% paraformaldehyde (PFA). Brains were post-fixed in PFA at 4°C for 24 hours, and then placed in 30% sucrose for 48 hours. Frozen coronal sections (50 µm) were cut on a sliding microtome, collected serially, placed in 200 µL of cryoprotectant (containing glycerin, ethylene glycol, and 0.1 m sodium-phosphate buffer, pH 7.4), and stored at −20°C. These were processed as free-floating sections and stained with DAPI (MP Biomedicals). Nuclei visualization as well as GFP expression at the viral injection site in the RSC and accurate miniscope placement were confirmed using an Olympus slide scanner VS200 microscope with a 10 x objective.

Data acquisition and preprocessing

In experiments involving solely behavior data acquisition - the WT behavioral imaging was recorded with a FLIR Blackfly S camera and SpinView software, while the apoE experiment was imaged using Thorcam software. Behavioral data was labeled (nose, midline top, midline middle and tail base) using a locally pre-trained DeepLabCut (RRID:SCR_021391) [17] network. DeepLabCut outputs pose estimation data in .h5 format, containing X and Y pixel coordinates along with likelihood scores for each labeled body part, which serves as input for the NaviGraph pipeline. For combined neuronal and behavioral imaging, behavior data was recorded at 30 fps using the FLIR setup mentioned above, triggered by and synchronized with the UCLA V4 miniscope data acquisition (DAQ) system [34]. Calcium imaging data from the miniscope were captured at matched fps using the Miniscope DAQ software [64], and neuronal activity traces were extracted with the Minian pipeline (RRID:SCR_022601) [65].

Head orientation analysis

Head orientation angles, stored along miniscope data in quaternion, were transformed locally to Euler angles (yaw, pitch, roll) with the SciPy Rotation library (RRID:SCR_008058) [66]. To prevent discontinuities at the ±180° boundary, angles were transformed into Cartesian coordinates, and then converted back for angular analysis. The yaw angle only was used for current head direction calculations. In order to obtain the phase offset between the sensor reference frame and the experimental reference frame, the linear equation between the positions of the 3 midline body parts of the mouse that did not include the nose was calculated for each frame (midline top, midline middle and tail-base). Logically, when all body parts tagged in this dataset are aligned the mouse should be looking straight ahead. Accordingly, we extracted the mean yaw angle for frames in which the nose was positioned along the computed linear equation when the mouse is facing the root node of the maze, resulting in the reference value. Processed yaw values were synchronized and integrated into NaviGraph's graph framework, enabling analysis of head orientation in relation to behavior and neuronal activity at decision points and paths.

Navigraph

NaviGraph is a modular Python-based pipeline designed for processing and analyzing behavioral, neuronal, and physiological data within maze paradigms using a graph-based framework (Fig. 1). Its modular structure allows for straightforward adjustments to fit various maze designs and data streams, with customizable analysis parameters and visualization outputs. Further details regarding installation, analysis, modulation and specific functions can be found in the GitHub repository https://github.com/PBLab/NaviGraph.

Configuration: Before executing the pipeline, experimental parameters and data paths are specified, including file paths for behavioral videos, maze maps, output directories, graph properties and spatial registration methods, in order to tailor the pipeline to specific experimental needs.

Calibration: Behavioral data are aligned with the maze map through a transformation matrix derived from user-selected reference points. This step ensures accurate spatial registration of trajectories within the experimental setup. Calibration is performed as follows:

1. Reference point selection: The user manually assigns corresponding reference points on the behavioral video and the maze map.
2. Transformation matrix computation: A transformation matrix is calculated to enable consistent spatial alignment across sessions.
3. Registration testing: To validate the calibration, newly selected points on the behavioral video are transformed using the computed matrix and overlaid onto the maze map for visual inspection.

Data visualization: NaviGraph provides a dedicated visualization module that enables simultaneous overlay of the extracted trajectory onto the behavioral video, maze map, and maze graph (e.g., a binary tree).

Data processing and integration: Following calibration, behavioral data are spatially registered to the maze structure and synchronized with neuronal and physiological recordings. The pipeline generates a structured dataset integrating the following data streams:

- Pose estimation: Extraction of x, y pixel coordinates and likelihood scores from pose estimation outputs.

- Maze position: Conversion of raw position data into discretized maze regions using a spatial tiling approach, ensuring systematic trajectory segmentation.

- Graph position: Mapping of maze tiles to a topological graph, where nodes represent decision points and edges define paths.

- Neuronal and physiological coupling: Synchronization of neuronal activity from calcium imaging with behavioral frames, along with head direction and any other physiological parameters.

Data analysis: NaviGraph facilitates the computation of both classic behavioral measurements and graph-based metrics. Results are aggregated and stored in a new dataset, where each row corresponds to an experimental session and columns represent results of behavioral metrics. The key analytical components include:

Topological metrics:

- **Cumulative path length:** Number of nodes traversed between any two points, giving a topological understanding of the animal's movement along the maze. As a benchmark of random navigation for the purpose of this study, we used the average cumulative number of nodes on the path to reward passed by 5000 random walk bouts on the graph with backtracking allowed only when no forward walking options exist (averaged 485.38 nodes in this case) relative to the perfect direct route to the reward (6 nodes).

- **Wandering Index:** Ratio of unique nodes traversed to the total number of nodes in the graph, providing a measure to the exploratory nature of the animal's trajectory. The random walker average (72.019 unique nodes in this case) relative to the perfect route was calculated in a similar manner to the previous metric.

- **Direct path to reward:** Calculates the longest uninterrupted sequence of nodes along the direct path the animal took towards the reward. This includes allowances for a set number of permitted deviations as specified by the user, making this metric highly flexible to accommodate many forms and limitations of mouse behavior around branches of the physical maze.

- **Average time at node:** Aggregation of time spent at each decision point, divided by visit frequency, to determine average dwell time.

Classical behavioral metrics:

- **Time and velocity analysis:** Computation of transition time and average movement speed between positions in the maze.

- **Exploration percentage:** Calculation of the proportion of unique nodes visited from the total number of nodes in the graph, providing a measure of maze coverage.

Customizable analysis: The modular structure of NaviGraph allows for easy integration of additional user-defined behavioral, neuronal or physiological analysis metrics tailored to specific research questions.

- **Result aggregation and visualization:** Tools for data aggregation by experimental groups and sessions and advanced plotting in various formats are incorporated following analysis.

Statistical analysis

For two-group comparisons in Navigraph behavioral metrics (male vs female WT mice Fig. 2c), Repeated Measures ANOVA test with Tukey's correction for multiple comparisons was used in the learning session trials, and the Mann-Whitney U test was applied in the memory session comparisons. For multi-group comparisons (apoE3 and apoE4 across genders Fig. 3c), in the learning session (between L1 and L4 trials) a mixed-effects model with Tukey's correction for multiple comparisons was used, and in the memory session the Kruskal-Wallis test followed by the two-stage step-up method of Benjamini, Krieger and Yekutieli for multiple comparison correction was used. Linear regression and the Kolmogorov-Smirnov test were applied for confidence index and visitation frequency relationship assessment and distribution analysis, respectively (Fig. 4a, d). For comparing neuronal activity data while moving or stationary, first normality was confirmed using the Shapiro-Wilk test following which a paired t-test was used for comparisons. The Ward method was applied for hierarchical clustering of neurons with similar activity patterns in different iterations to the same path, followed by the Mann-Whitney U test with a Bonferroni correction for multiple comparisons of clusters. Statistical analysis was performed using GraphPad Prism 10 (RRID:SCR_002798), as well as Python's SciPy (RRID:SCR_008058) [66] and Statsmodels (RRID:SCR_016074) [67] libraries, with a significance threshold of $p < 0.05$.

Author contributions

AKI, DMM and PB designed the study. AKI and PB designed and built the setup. AKI performed experiments, collected and analyzed data. EI and AKI developed the software pipeline. AKI and PB wrote the manuscript. DMM and PB provided financial support and mentoring.

Acknowledgements

The authors would like to thank Eran Rosen and the staff at the Mechanical Workshop of the School of Chemistry and Physics at Tel-Aviv University for manufacturing the maze, and Dr. Anton Sheinin from the Sagol School of Neuroscience for designing the maze automation hardware. We would also like to thank Dr. David Kain for valuable input regarding surgery, Rotem Yam-Shahor for imaging brain slices, Lior Lin and Omri Koren for help in the behavioral experiments, as well as Dr. Lior Bikovski and the Myers Neuro-Behavioral Core Facility for providing T-maze behavioral imaging. PB wants to thank the La Caixa Foundation (grant No. HR23-00560) and Israeli Science Foundation (grant No. 2342/21) for financial support. AKI wants to thank The Prajs-Drimmer Institute for the Development of Anti-Degenerative Drugs for scholarship support.

References

1. Ghafarimoghadam, M. *et al.* A review of behavioral methods for the evaluation of cognitive performance in animal models: Current techniques and links to human cognition. *Physiol. Behav.* **244**, 113652 (2022).
2. Zhang, R. *et al.* The pros and cons of motor, memory, and emotion-related behavioral tests in the mouse traumatic brain injury model. *Neurol. Res.* **44**, 65–89 (2022).
3. Guo, Z. V. *et al.* Procedures for Behavioral Experiments in Head-Fixed Mice. *PLoS ONE* **9**, e88678 (2014).
4. Giovannucci, A. *et al.* Automated gesture tracking in head-fixed mice. *J. Neurosci. Methods* **300**, 184–195 (2018).
5. Kendall-Bar, J. M. *et al.* Brain activity of diving seals reveals short sleep cycles at depth. *Science* **380**, 260–265 (2023).
6. Vogt, C. C. *et al.* Female behavior drives the formation of distinct social structures in C57BL/6J versus wild-derived outbred mice in field enclosures. *BMC Biol.* **22**, 35 (2024).
7. Multiscale representation of very large environments in the hippocampus of flying bats | Science. https://www.science.org/doi/10.1126/science.abg4020.
8. Rosenberg, M., Zhang, T., Perona, P. & Meister, M. Mice in a labyrinth show rapid learning, sudden insight, and efficient exploration. *eLife* **10**, e66175 (2021).
9. Small, W. S. Experimental study of the mental process of the rat. II. *Am. J. Psychol.* **12**, 206–239 (1901).
10. A history of ‘maze’ psychology | Why People Get Lost: The Psychology and Neuroscience of Spatial Cognition | Oxford Academic. https://academic.oup.com/book/5747/chapter-abstract/148887317?redirectedFrom=fulltext.
11. Maguire, E. A., Burgess, N. & O’Keefe, J. Human spatial navigation: cognitive maps, sexual dimorphism, and neural substrates. *Curr. Opin. Neurobiol.* **9**, 171–177 (1999).
12. Lupien, S. J., McEwen, B. S., Gunnar, M. R. & Heim, C. Effects of stress throughout the lifespan on the brain, behaviour and cognition. *Nat. Rev. Neurosci.* **10**, 434–445 (2009).
13. Sandi, C. Stress and cognition. *Wiley Interdiscip. Rev. Cogn. Sci.* **4**, 245–261 (2013).

14. Chazal, F. & Michel, B. An Introduction to Topological Data Analysis: Fundamental and Practical Aspects for Data Scientists. *Front. Artif. Intell.* **4**, (2021).
15. Zong, W. *et al.* Large-scale two-photon calcium imaging in freely moving mice. *Cell* **185**, 1240-1256.e30 (2022).
16. Aharoni, D. & Hoogland, T. M. Circuit Investigations With Open-Source Miniaturized Microscopes: Past, Present and Future. *Front. Cell. Neurosci.* **13**, 141 (2019).
17. Nath, T. *et al.* Using DeepLabCut for 3D markerless pose estimation across species and behaviors. *Nat. Protoc.* **14**, 2152–2176 (2019).
18. de Chaumont, F. *et al.* Real-time analysis of the behaviour of groups of mice via a depth-sensing camera and machine learning. *Nat. Biomed. Eng.* **3**, 930–942 (2019).
19. Chen, Z. *et al.* Automated, high-dimensional evaluation of physiological aging and resilience in outbred mice. *eLife* **11**, e72664.
20. Uludağ, K. & Roebroeck, A. General overview on the merits of multimodal neuroimaging data fusion. *NeuroImage* **102**, 3–10 (2014).
21. Large-scale neural recordings call for new insights to link brain and behavior | Nature Neuroscience. https://www.nature.com/articles/s41593-021-00980-9.
22. Tegtmeier, J. *et al.* CAVE: An Open-Source Tool for Combined Analysis of Head-Mounted Calcium Imaging and Behavior in MATLAB. *Front. Neurosci.* **12**, 958 (2018).
23. Brand, Z. & Avital, A. High resolution behavioral and neural activity representation using a geometrical approach. *Sci. Rep.* **10**, 7977 (2020).
24. Multilayer networks | Journal of Complex Networks | Oxford Academic. https://academic.oup.com/comnet/article/2/3/203/2841130?login=true.
25. All the light that we can see: a new era in miniaturized microscopy | Nature Methods. https://www.nature.com/articles/s41592-018-0266-x.
26. Citric Acid Water as an Alternative to Water Restriction for High-Yield Mouse Behavior | eNeuro. https://www.eneuro.org/content/8/1/ENEURO.0230-20.2020.
27. Reinagel, P. Training Rats Using Water Rewards Without Water Restriction. *Front. Behav. Neurosci.* **12**, (2018).

28. Reddy, G. A reinforcement-based mechanism for discontinuous learning. *Proc. Natl. Acad. Sci.* **119**, e2215352119 (2022).
29. Tolman, E. C. Cognitive maps in rats and men. *Psychol. Rev.* **55**, 189–208 (1948).
30. From cognitive maps to spatial schemas | Nature Reviews Neuroscience. https://www.nature.com/articles/s41583-022-00655-9.
31. Fortea, J. *et al.* APOE4 homozygosity represents a distinct genetic form of Alzheimer's disease. *Nat. Med.* **30**, 1284–1291 (2024).
32. van Heuvelen, M. J. G., van der Lei, M. B., Alferink, P. M., Roemers, P. & van der Zee, E. A. Cognitive deficits in human ApoE4 knock-in mice: A systematic review and meta-analysis. *Behav. Brain Res.* **471**, 115123 (2024).
33. Salomon-Zimri, S., Liraz, O. & Michaelson, D. M. Behavioral testing affects the phenotypic expression of *APOE* ε3 and *APOE* ε4 in targeted replacement mice and reduces the differences between them. *Alzheimers Dement. Diagn. Assess. Dis. Monit.* **1**, 127–135 (2015).
34. Home · Aharoni-Lab/Miniscope-v4 Wiki · GitHub. https://github.com/Aharoni-Lab/Miniscope-v4/wiki.
35. Alexander, A. S., Place, R., Starrett, M. J., Chrastil, E. R. & Nitz, D. A. Rethinking retrosplenial cortex: Perspectives and predictions. *Neuron* **111**, 150–175 (2023).
36. Maze miniscope | BioRender. https://app.biorender.com/citation/67a208b292fa4065474eddc0.
37. O'Keefe, J. & Nadel, L. *The Hippocampus as a Cognitive Map*. *Oxford University Press: Oxford, UK. (1978)* (Oxford University Press, Oxford, UK, 1978).
38. Vorhees, C. V. & Williams, M. T. Value of water mazes for assessing spatial and egocentric learning and memory in rodent basic research and regulatory studies. *Neurotoxicol. Teratol.* **45**, 75–90 (2014).
39. Duarte-Guterman, P., Yagi, S., Chow, C. & Galea, L. A. M. Hippocampal learning, memory, and neurogenesis: Effects of sex and estrogens across the lifespan in adults. *Horm. Behav.* **74**, 37–52 (2015).

40. Vorhees, C. V. & Williams, M. T. Assessing Spatial Learning and Memory in Rodents. *ILAR J.* **55**, 310–332 (2014).
41. Yuan, L. *et al.* Gender Differences in Large-Scale and Small-Scale Spatial Ability: A Systematic Review Based on Behavioral and Neuroimaging Research. *Front. Behav. Neurosci.* **13**, 128 (2019).
42. Gire, D. H., Kapoor, V., Arrighi-Allisan, A., Seminara, A. & Murthy, V. N. Mice develop efficient strategies for foraging and navigation using complex natural stimuli. *Curr. Biol. CB* **26**, 1261–1273 (2016).
43. Network analysis of exploratory behaviors of mice in a spatial learning and memory task | PLOS ONE. https://journals.plos.org/plosone/article?id=10.1371/journal.pone.0180789.
44. Pfeiffer, B. E. & Foster, D. J. Hippocampal place-cell sequences depict future paths to remembered goals. *Nature* **497**, 74–79 (2013).
45. Derdikman, D. & Moser, M.-B. A Dual Role for Hippocampal Replay. *Neuron* **65**, 582–584 (2010).
46. Reconceiving the hippocampal map as a topological template | eLife. https://elifesciences.org/articles/3476.
47. Fang, W. *et al.* APOE4 genotype exacerbates the depression-like behavior of mice during aging through ATP decline. *Transl. Psychiatry* **11**, 1–9 (2021).
48. Leung, L. *et al.* Apolipoprotein E4 causes age- and sex-dependent impairments of hilar GABAergic interneurons and learning and memory deficits in mice. *PloS One* **7**, e53569 (2012).
49. Jochemsen, H. M., Muller, M., van der Graaf, Y. & Geerlings, M. I. APOE ε4 differentially influences change in memory performance depending on age. The SMART-MR study. *Neurobiol. Aging* **33**, 832.e15-832.e22 (2012).
50. Xiong, J. *et al.* FSH and ApoE4 contribute to Alzheimer's disease-like pathogenesis via C/EBPβ/δ-secretase in female mice. *Nat. Commun.* **14**, 6577 (2023).

51. Altmann, A., Tian, L., Henderson, V. W., Greicius, M. D., & Alzheimer's Disease Neuroimaging Initiative Investigators. Sex modifies the APOE-related risk of developing Alzheimer disease. *Ann. Neurol.* **75**, 563–573 (2014).
52. Ungar, L., Altmann, A. & Greicius, M. D. Apolipoprotein E, gender, and Alzheimer's disease: an overlooked, but potent and promising interaction. *Brain Imaging Behav.* **8**, 262–273 (2014).
53. Cheng, N. *et al.* Egocentric processing of items in spines, dendrites, and somas in the retrosplenial cortex. *Neuron* **112**, 646-660.e8 (2024).
54. Park, K., Yeo, Y., Shin, K. & Kwag, J. Egocentric neural representation of geometric vertex in the retrosplenial cortex. *Nat. Commun.* **15**, 7156 (2024).
55. Elduayen, C. & Save, E. The retrosplenial cortex is necessary for path integration in the dark. *Behav. Brain Res.* **272**, 303–307 (2014).
56. Cooper, B. G. & Mizumori, S. J. Retrosplenial cortex inactivation selectively impairs navigation in darkness. *Neuroreport* **10**, 625–630 (1999).
57. Epstein, R. A., Patai, E. Z., Julian, J. B. & Spiers, H. J. The cognitive map in humans: Spatial navigation and beyond. *Nat. Neurosci.* **20**, 1504–1513 (2017).
58. Laboratory, I. B. *et al.* Reproducibility of in vivo electrophysiological measurements in mice. *eLife* **13**, (2025).
59. Jun, J. J. *et al.* Fully integrated silicon probes for high-density recording of neural activity. *Nature* **551**, 232–236 (2017).
60. Sullivan, P. M. *et al.* Targeted replacement of the mouse apolipoprotein E gene with the common human APOE3 allele enhances diet-induced hypercholesterolemia and atherosclerosis. *J. Biol. Chem.* **272**, 17972–17980 (1997).
61. Bar, R., Boehm-Cagan, A., Luz, I., Kleper-Wall, Y. & Michaelson, D. M. The effects of apolipoprotein E genotype, α-synuclein deficiency, and sex on brain synaptic and Alzheimer's disease-related pathology. *Alzheimers Dement. Amst. Neth.* **10**, 1–11 (2018).
62. Thingiverse.com. Simple Syringe Pump by doctek. *Thingiverse* https://www.thingiverse.com/thing:866904.

63. Benbenishty, A. *et al.* Longitudinal in vivo imaging of perineuronal nets. *Neurophotonics* **10**, 015008 (2023).

64. GitHub - Aharoni-Lab/Miniscope-DAQ-QT-Software: Software for streaming and controlling neural and behavioral data from freely behaving animals. https://github.com/Aharoni-Lab/Miniscope-DAQ-QT-Software.

65. Dong, Z. *et al.* Minian, an open-source miniscope analysis pipeline. *eLife* **11**, e70661 (2022).

66. Virtanen, P. *et al.* SciPy 1.0: fundamental algorithms for scientific computing in Python. *Nat. Methods* **17**, 261–272 (2020).

67. Seabold, S. & Perktold, J. Statsmodels: Econometric and Statistical Modeling with Python. *Proc. 9th Python Sci. Conf.* 92–96 (2010) doi:10.25080/Majora-92bf1922-011.

68. *Complex Maze Paradigm Hardware Setup*.

Supplementary

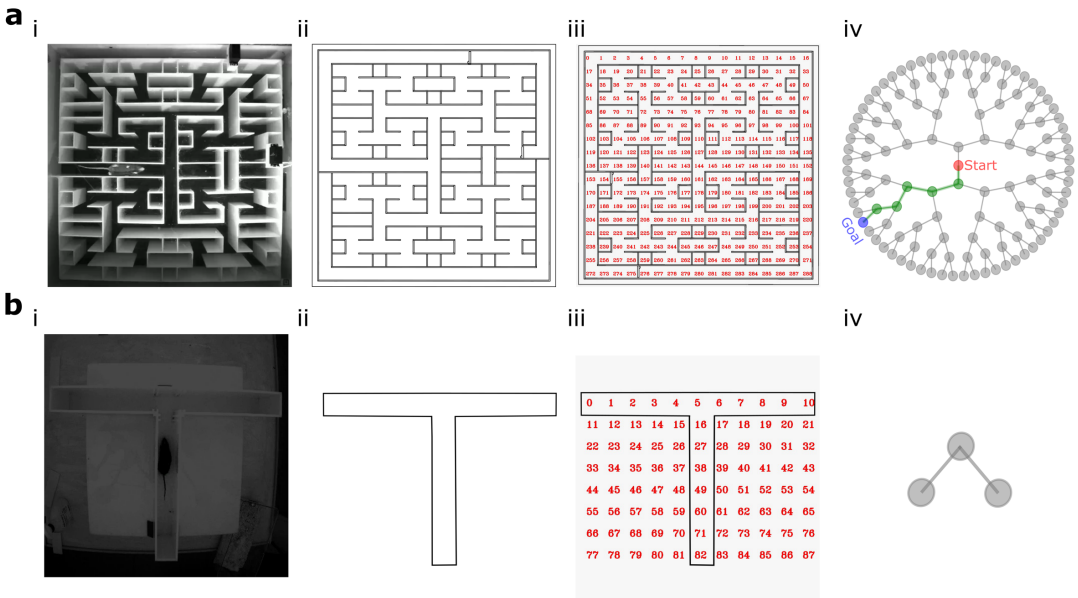

Supplementary figure 1: NaviGraph pipeline flexibility. *(a) The complex maze setup. A workflow displaying: (i) Raw behavioral imaging. (ii) Corresponding schematic representation of the maze structure. (iii) NaviGraph tiles depicting the numbered grid overlay for each maze region. (iv) NaviGraph corresponding graph representation of the maze. The green-highlighted path marks the shortest route from the starting point (red) to the goal (blue). (b) T-maze setup as an example of NaviGraph flexibility for additional maze structures. (i) Raw imaging data from T-maze behavioral experiment, (ii) Schematic map of the T-maze structure, (iii) NaviGraph tiles assigning numbers to discrete regions. (iv) Corresponding graph representation of the T-maze.*

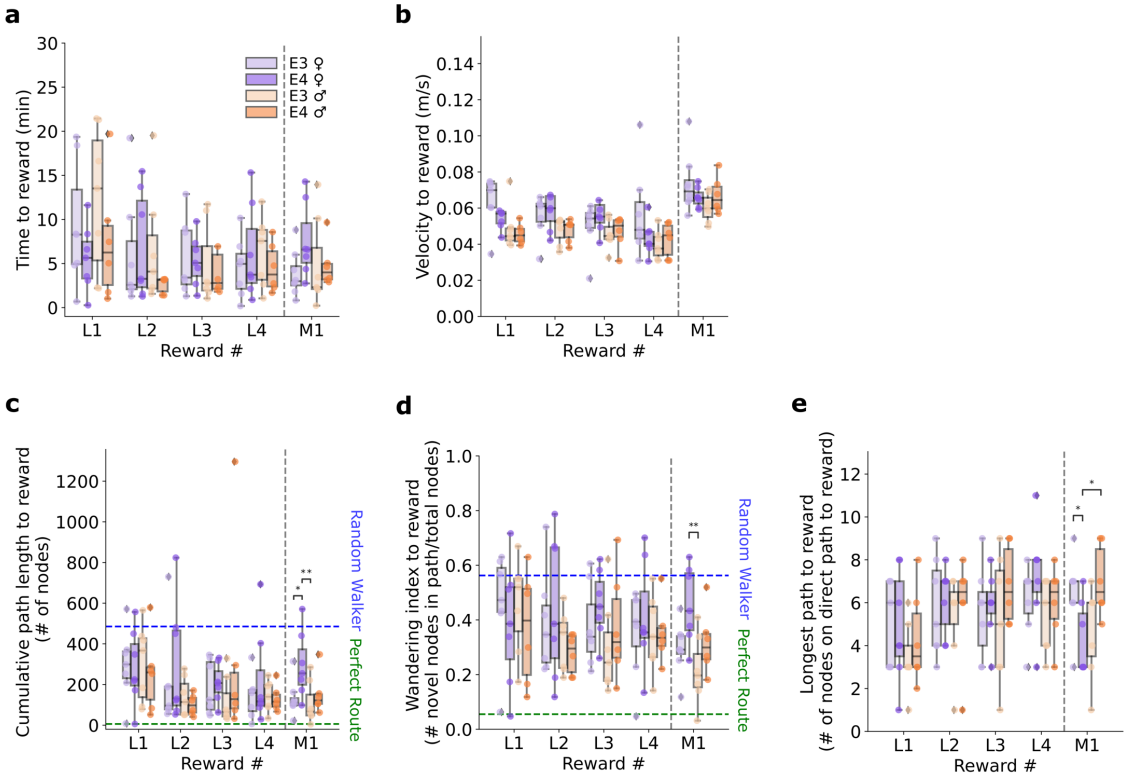

***Supplementary figure 2**: **NaviGraph behavioral analysis of apoE4 and apoE3 male and female mice.** ApoE4 and control apoE3 targeted replacement 5-month-old female (n=7-8) and male (n=6-7) mice received ad-libitum citric acid water for one week followed by a learning and post 72h memory session in the complex maze paradigm. (a-e) NaviGraph behavioral classic and topological metrics. Plots depict results for the learning session trials (L1, L2, L3, L4) and the memory session (M1). Females and males shown in purple and orange, respectively, apoE4 genotype in darker shades. (a) Time to reward. (b) Average velocity to the reward. (c) Cumulative path length, total number of nodes passed to reach reward. Average of 5000 random walker bouts on the graph depicted by the blue dashed line. Direct path to reward depicted in green dashed line. (d) Wandering index, number of unique nodes passed to reach reward. (e) Longest direct path to reward, number of graph nodes passed on the direct path to the reward. Data depicted as median ± interquartile range; * p<0.05, ** p<0.01.*

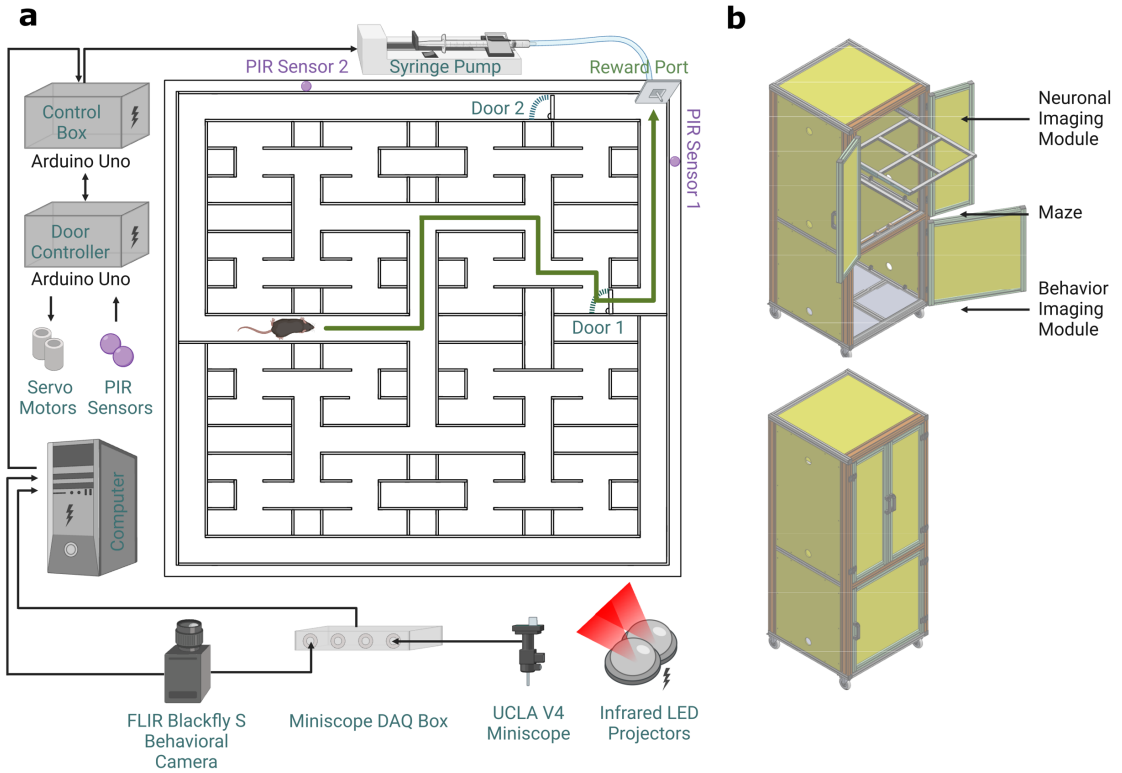

Supplementary figure 3*: *Complex maze paradigm hardware setup. *(a) Schematic of the hardware components supporting the complex maze paradigm. (b) Self-contained chamber designed for behavioral and neuronal imaging of complex maze apparatus. Created with BioRender* [68].